Materials Characterization 169 (2020) 110651

Contents lists available at ScienceDirect

Materials Characterization

journal homepage: www.elsevier.com/locate/matchar

Nucleation of W-rich carbides and Laves phase in a *Re*-containing 10% Cr steel during creep at 650 °C

A. Fedoseeva*, I. Nikitin, N. Dudova, R. Kaibyshev

Belgorod National Research University, Pobeda 85, Belgorod 308015, Russia

ARTICLE INFO

Keywords:
Steel
Electron microscopy
Precipitation
Phase transformation
Orientation relationships

ABSTRACT

The nucleation of the Laves phase particles in a *Re*-containing 10% wt. Cr-3% Co-3% W steel with a low nitrogen and a high boron contents during creep is characterized by distinctive features. The precipitation process can be written as $M_{23}C_6$ carbide → M_6C carbide → Laves phase. The nucleation of all phases in this precipitation sequence is heterogeneous. The $M_{23}C_6$ carbides precipitate on the boundaries of martensitic structure during tempering at temperature of 770 °C. The M_6C (Fe_3W_3C) carbides precipitate during both tempering at 770 °C and creep at 650 °C on the $M_{23}C_6$/ferrite surfaces and on the martensitic lath boundaries. The M_6C carbides have the mutual relationship of crystal orientations with both the $M_{23}C_6$ carbides and ferrite. The chemical composition of the M_6C carbides depends on their nucleation sites. After 83 h of creep, the M_6C carbides starts to dissolve, whereas the Laves phase particles are nucleated on the M_6C/ferrite surface and separately on the martensitic lath boundaries. The Laves phase particles nucleate on the M_6C/ferrite surface are smaller than those nucleated on the martensitic lath boundaries. The Laves phase particles exhibit the unique orientation relationships with a high misfit. The transformation of $M_{23}C_6$ → M_6C → Laves phase is an in-situ transformation accompanied by chemical compositional changes.

1. Introduction

The efficiency of fuel fossil power plants can be enhanced by increasing the parameters such as temperature and pressure [1–4]. Main problem, which is related to an increase in temperature up to 620 °C, is the lack of heat-resistant materials with the high creep properties, certain fracture toughness, fatigue resistance, joinability, oxidation/corrosion resistance etc. together with acceptable cost [1,2]. So, the required creep strength for new materials is 100 MPa at a service temperature over a time period of 100,000 h without fracture [1,5]. The 9–12% Cr ferritic and martensitic steels (the P92 and P122 types) are the prospective candidates for the elements of power plants working at 600–620 °C [1–5]. Normalizing at 1050–1100 °C followed by tempering at temperatures ranging from 720 to 800 °C produces the tempered martensitic lath structure (TMLS) composed of a hierarchical sequence of the structural elements, i.e. prior austenite grains (PAGs), packets, blocks and martensitic laths with a high density of free dislocations [2,6,7]. Superior creep resistance of these steels is attributed to stability of the TMLS provided by secondary phase particles, which should impede the knitting reactions between the lattice dislocations and lath boundaries and exert a high Zener drag pressure [2,6,8–14]. Three types of secondary phase particles contribute to stability of the TMLS [2,6,9–14]. The boundary $M_{23}C_6$ carbides precipitated during tempering and Laves phase precipitated during creep/ageing give the main contribution to the Zener drag pressure, and MX carbonitrides precipitated in the ferritic matrix effectively pin the lattice dislocations hindering the knitting reaction [9–14]. The strain-induced coarsening of the $M_{23}C_6$ carbides and replacement of the fine MX carbonitrides by coarse *Z*-phase (CrVN) lead to evolution of the TMLS into the subgrain structure [9–18].

It was recently shown [10,15,18–25] that Laves phase plays an important role in creep behavior of the steels with the low N and high B contents, since the coarsening rate of the $M_{23}C_6$ carbides is low and the transformation of the MX into the *Z*-phase is unimportant for such type of the high-Cr steels. The precipitation and coarsening of the Laves phase particles contribute to the creep strength [15,18,21,25–31]. On one hand, precipitation of the Laves phase particles on the martensitic lath boundaries during the transition creep stage results in strengthening and decreasing a steady-state creep rate that increases the creep strength [12,15,18]. The chains of these particles effectively pin the lattice dislocations restricting in-lath slip and hindering the recovery of dislocations within the lath boundaries that contributes to the threshold stress and retards the onset of steady-state creep stage [12,15,18,27,32–34]. The fine Laves phase particles induce the high

* Corresponding author.
E-mail address: fedoseeva@bsu.edu.ru (A. Fedoseeva).

https://doi.org/10.1016/j.matchar.2020.110651
Received 25 May 2020; Received in revised form 10 September 2020; Accepted 13 September 2020
Available online 16 September 2020
1044-5803/

Zener drag pressure preventing the lath boundary migration [9,11,13,14,21,35–38]. As a result, the chains of the Laves phase particles along the lath and block boundaries provide effective stabilization of the TMLS during the creep testing.

On the other hand, the Laves phase particles are susceptible to coarsening during the steady-state and tertiary creep stages that leads to dissolution of the fine particles on the lath and block boundaries and growth of the coarse particles on the boundaries of packets and PAGs [19,22]. This accelerates transformation of the TMLS into the subgrain structure [15,21,22,31]. The Laves phase precipitation leads to the depletion of W and Mo from the solid solution that increases diffusivity and reduces solid solution strengthening that facilitates dislocation climb and glide [9,21,31]. Moreover, the coarse Laves phase particles located on the PAG boundaries act as the cavity nucleation sites, initiating damage that decreases the strain to rupture and causes premature fracture [9,11,28,36,37,39].

The nucleation of the Laves phase particles is always heterogeneous on the boundaries of all structural elements including the martensitic laths [2,8–11,13–15,18,19,21,22,26,28,29,35–47]. The boundary $M_{23}C_6$ carbides highly facilitate the Laves phase nucleation on high-angle boundaries promoted by W or Mo segregations [26,40,45]. A specific nucleation of Laves phase takes place in the high-Cr steels with the high W content or/and the high B and low N contents. The precipitation of Laves phase occurs through the transitional M_6C carbide [10,11,45,48]. The total precipitation sequence for these steels can be written as:

$$M_{23}C_6 \rightarrow M_6C \rightarrow \text{Laves phase} \quad (1)$$

It is known that W-rich M_6C (Fe_3W_3C) carbide has the cubic type crystal structure with a lattice parameter of ~1.109 nm. Laves phase can replace M_6C carbide due to either a nucleation on interface boundaries of existing M_6C carbides, or transformation of cubic lattice of M_6C into a hexagonal one of Laves phase [48]. The formation of M_6C carbides followed by their transformation to Laves phase is promoted by boundary segregations of W or Mo [45]. However, features of this process are poorly known [10,11,15,44–46,48,49]. There are a lot of studies focused on investigation of evolution of Laves phase during long-term ageing and creep [2,9–11,13–15,18,21–23,26–43,46,47,49,50], but the precipitation sequence (1) is open question. Moreover, the nucleation of W-rich M_6C carbides and their effect on the precipitation of Laves phase in the high-Cr steels have not been studied in detail. So, the first aim of the present research is to report on the nucleation behavior of the W-rich carbides and Laves phase. The investigation of nucleation process which determines the coarsening behavior of Laves phase is important since evolution of Laves phase affect the creep strength properties of the high-Cr steels with the high B and low N contents [25].

In the previous research [23,25], it has been found that a significant portion of the Laves phase particles precipitates on the lath boundaries instead of high-angle boundaries of PAGs, blocks and/or packets during transient creep in the *Re*-containing 10% Cr steel; such dominant nucleation of Laves phase on the low-angle lath boundaries is non-typical for the 9–10% Cr steels [10,11,15,23,25,49]. Moreover, the coarsening of these particles of Laves phase occurs with low rate; the chains of these particles on the lath boundaries retained up to rupture even after 10^4 h that provide the improved creep resistance under the high applied stresses in comparison with the *Re*-free 9–10%Cr steels [23,25]. The second aim of the present study is to reveal the reasons of the precipitation of Laves phase on the low-angle lath boundaries, mainly, in the 10% Cr steel with 3% Co, 3% W and 0.2% Re additives under short-term creep ($\leq$ 440 h) at 650 °C.

2. Material and Methods

A steel, which is denoted here as *Re*-containing 10% Cr-3% Co-3% W, with the chemical composition of (in wt%) Fe (bal.)–0.11C–9.85Cr–3.20Co–2.86 W-0.13Mo–0.22Cu-0.03Si–0.14Mn–0.03Ni-0.23 V–0.07Nb–0.002 N–0.008B-0.17Re, was prepared by vacuum induction melting as 100 kg ingot. Square bars with a 11 mm × 11 mm cross-section were cast and hot forged. Next, this steel was normalized at 1050 °C for 1 h and tempered at 770 °C for 3 h. Creep tests were carried out at 650 °C with applied stress ranging from 130 to 200 MPa. Flat specimens with a gage length of 25 mm and a cross section of 7 mm × 3 mm were crept at 650 °C under the applied stresses of 160, 180 and 200 MPa until rupture. Under an applied stress of 130 MPa, the creep test was interrupted after 254 h, which corresponded to 1% creep strain. The creep conditions together with testing creep time are summarized in Table 1.

Table 1
Creep time for tests used in the present investigation.

Nominal stress, MPa	200 Ruptured	180 Ruptured	130 Interrupted	160 Ruptured	140 Ruptured
Time, h	8	83	254	440	10,987

The structural characterization of crept samples was carried out using a transmission electron microscope JEOL–2100 (TEM) with an INCA energy dispersive X-ray spectrometer (EDS) on ruptured and interrupted creep specimens. Identification of the precipitates was performed based of combination of EDS composition measurements of the metallic elements and indexing of the electron diffraction patterns using TEM. The TEM specimens were prepared by electropolishing at room temperature using a solution of 10% perchloric acid in glacial acetic acid with Struers «Tenupol-5» machine. The precipitates were identified from both the chemical analysis and the selected-area diffraction method on at least 100 particles on the each portion using extraction carbon replicas. The carbon replicas were prepared using Q 150REQuorum vacuum deposition machine. The equilibrium chemical composition of Laves phase was obtained using Thermo-Calc software. The particle coarsening kinetic was calculated using Prisma-software on the base of Calphad Database Calculation with the kinetic MOBFE1 and thermodynamic TCFE6 databases. The model composition consisting of Fe, C, Cr, Mo, W and Co in accordance with the chemical composition of the steel studied was used. The time dependencies of the mean radius and volume fraction were determined for M_6C carbides and Laves phase particles assuming the simultaneous growth of $M_{23}C_6$ carbides, M_6C carbides and Laves phase; a grain boundary acted as a nucleation site. The other details of mechanical and structural characterization technique were presented in previous studies [9–11,13–15,21,23,25,32,33,36,37,45,46,48–50].

3. Results and Discussion

3.1. Tempered Structure

Microstructure and a distribution of secondary phase particles in the *Re*-containing 10% Cr-3% Co-3% W steel after normalizing at 1050 °C and tempering at 770 °C were considered in previous works [23,25] in some details. An average PAG size was 59 μm; an average width of the martensitic laths containing a high dislocation density of 2×10^{14} m^{-2} in their interiors was 290 ± 30 nm (Fig. 1a). The boundaries of PAGs, packets, blocks and laths were decorated by Cr-rich $M_{23}C_6$ carbides with a mean size of 67 nm (Fig. 1a). Nb-rich MX carbonitrides with a mean size of 37 nm were homogeneously distributed in the ferritic matrix (Fig. 1a). Additionally, W-rich M_6C (Fe_3W_3C) carbides were found to locate along the martensitic lath boundaries and preferentially together with the $M_{23}C_6$ carbides (Fig. 1b-d). Their mean size was 28 nm. The dimension of the M_6C carbides after 770 °C-tempering in the *Re*-free 10% Cr-3% Co-2% W steel [48] and the present steel is nearly the same, whereas the size of the M_6C carbides in the present steel is smaller by a factor of ~14 in comparison with the Re-free 9% Cr-3% Co-3% W steel containing 0.05% N and 0.005% B [45]. The M_6C

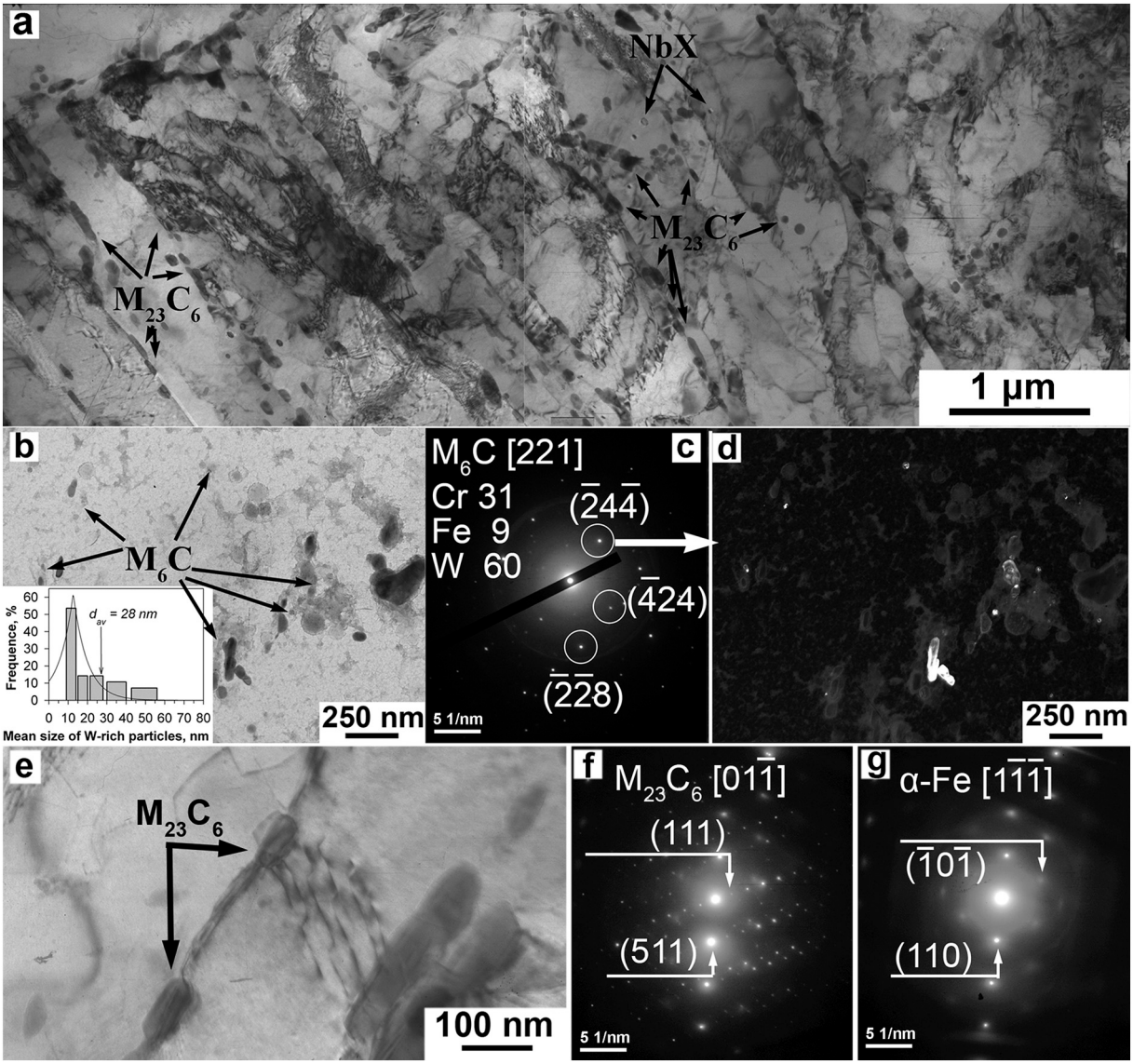

Fig. 1. The formation of tempered martensite lath structure after normalizing at 1050 °C with following tempering at 770 °C (a); bright-field TEM image of carbon replica showing M_6C carbides (b) and electron diffraction pattern from M_6C carbide (c) with corresponding dark-field image in reflection of M_6C carbide (d); bright-field TEM image of foil showing $M_{23}C_6$ carbides (e) and electron diffraction pattern from the $M_{23}C_6$ carbide (f) and the adjacent ferrite matrix (g).

carbides contained 60 wt% W, 31% Cr and 9% Fe (Fig. 1c). No evidence for the Laves phase precipitation during tempering in the Re-containing 10% Cr-3% Co-3% W steel was revealed by TEM analysis (Fig. 1). This fact is in contrast to a 9% Cr-3% Co-3% W steel [45], in which the Laves phase is formed under tempering in a case of isolation of M_6C carbides from W segregation by neighboring $M_{23}C_6$ particles.

Analysis of the selected area diffraction patterns (SAED) (Fig. 1e-g) showed that there were two types of orientation relationships (ORs) between the $M_{23}C_6$ carbides located on the lath boundaries and ferritic matrix (α). The $M_{23}C_6$ carbides exhibiting the Kurdjumov-Sachs OR with the matrix were in dominance and the OR could be written as [45]:

$$(110)_\alpha \| (111)_{M_{23}C_6},\ [1\bar{1}\bar{1}]_\alpha \| [01\bar{1}]_{M_{23}C_6} \quad (2)$$

The lattice misfit (δ) between the particles and ferritic matrix can be defined by [37,45]:

$$\delta = \frac{d_{particle} - d_\alpha}{d_\alpha} \quad (3)$$

where $d_{particle}$ and d_α are the interplanar spacing of the particle and ferritic matrix, respectively. In the Kurdjumov-Sachs OR, a $(110)_\alpha$ plane exhibits a good coincidence of ~1%, while the $(111)_\alpha$ and $(211)_\alpha$ planes exhibit misfits of ~8.9% and ~ 7.1%, respectively [51]. The $M_{23}C_6$ carbides with such OR had a plate-like shape with a broad semi-coherent interface being parallel to a $(110)_\alpha$ plane (Fig. 1e-g).

In addition, the $M_{23}C_6$ carbides were found with a specific OR defined by [51]:

$$(110)_\alpha \| (115)_{M_{23}C_6},\ [1\bar{1}\bar{1}]_\alpha \parallel [\bar{5}\ 10\ \bar{1}]_{M_{23}C_6} \quad (4)$$

This OR is a deviation from the Kurdjumov-Sachs OR due to the accumulation of dislocations at the $M_{23}C_6$/α-Fe interfaces [51]. The lattice misfit of the $M_{23}C_6$ carbides with the ORs from Eqs. (3) and (4) is characterized by the same value as well as the misfit along a $(110)_\alpha$ plane. It is worth noting that the OR described by Eq. (4) was found in a P911-type steel after creep and was explained in terms of a local strain incompatibility [51].

3.2. Evolution of M_6C Carbides During Creep

The W content in the solid solution reduced with creep time that

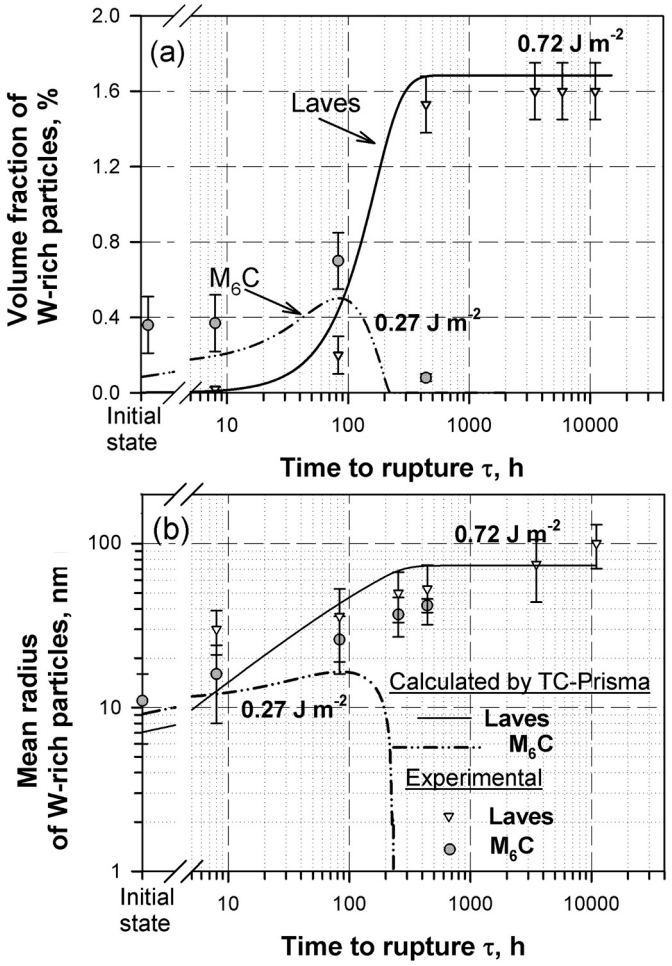

Fig. 2. Time dependence of the volume fraction (a) and particle size (b) of Laves phase and M_6C carbide during creep. Circle grey points and white triangle down are the experimental data and correspond to M_6C and Laves phase particles, respectively; dash-dot-dot and solid lines are the calculated curves obtained by Prisma-software for the model steel and correspond to the M_6C and Laves phase particles, respectively.

was accompanied with the precipitation of W-rich particles. The volume fractions and average sizes of W-rich particles estimated using TEM method are presented in Fig. 2a and b, respectively, by the experimental points. Also, the time dependencies of these parameters predicted by TC-Prisma software are presented by curves. The TEM experimental points and calculated lines predicted by TC-Prisma software had a good correlation for both M_6C carbides with an interfacial energy of 0.27 J m^{-2} and Laves phase with an interfacial energy of 0.72 J m^{-2}. The volume fraction of M_6C carbides with the interfacial energy of 0.27 J m^{-2} increased up to 0.5% with a maximal peak corresponding to 80 h, and then the volume fraction decreased down to 0 at 200–220 h. Experimental results showed the presence of M_6C carbides after 254 h and 440 h of creep, but their amount was negligible. According to the prediction by TC-Prisma software and experimental results, the equilibrium W content in the ferritic matrix of 1.24 wt% [23,25] and volume fraction of Laves phase of 1.6% was reached after 500 h of creep. A mean size of M_6C carbides increased from 28 nm in tempered state to 52 nm after 83 h of creep, and then these particles must be dissolved according to the line calculated using TC-Prisma software, whereas the experimental data showed the retaining separate M_6C carbides with the mean size of 80–85 nm after 440 h of creep (Fig. 2b). According to the calculating line predicted using TC-Prisma software for Laves phase with the interfacial energy of 0.72 J m^{-2}, the mean size of the Laves phase particles must increase up to 140 nm for 500 h of creep and then be constant for next 10,000 h. Experimental data agreed with calculating line (Fig. 2b): the mean size of Laves phase increased from 60 nm after 8 h of creep to 200 nm after 10,987 h of creep (Fig. 2b). The presence of the fine Laves phase particles along the martensitic lath boundaries and coarse Laves phase particles along the boundaries of packets, blocks and PAGs indicates the further growth of these particles with the possible increment in the interfacial energy as it was described for 9% Cr-3% Co-3% W steel [46].

There were two ways to observe M_6C carbides (Figs. 3 and 4):

- on the $M_{23}C_6$/ferrite surfaces (Figs. 3 and 5);
- on the martensitic lath boundaries (Figs. 4 and 5).

After 8 h of creep at 200 MPa, the M_6C carbides had a bimodal size distribution with the peaks corresponding to nucleation of the M_6C carbides on the $M_{23}C_6$/α-Fe surfaces (at a size of M_6C carbides of 10–20 nm) and on the martensitic lath boundaries (at 50–70 nm), respectively (Fig. 5a). After creep for 83 h at 180 MPa, the bimodal size distribution retained: the peak corresponding to nucleation of the M_6C carbides on the $M_{23}C_6$/α-Fe surfaces was enhanced and shifted to the side of 30–50 nm, whereas the peak corresponding to the nucleation of M_6C carbides on the martensitic lath boundaries became lower and was shifted to 100–120 nm (Fig. 5c). The number ratios between the M_6C carbides located on the martensitic lath boundaries and on the $M_{23}C_6$/α-Fe surface were 1: 3 and 1: 6 after creep tests at 200 MPa (8 h) and 180 MPa (83 h). The chemical compositions of the M_6C carbides located on the $M_{23}C_6$ carbides and martensitic lath boundaries were different (Fig. 6a and b). The M_6C located on the $M_{23}C_6$ carbides were enriched by Cr up to 20 wt% (Fig. 6a). The chemical composition of the M_6C carbides located on the martensitic lath boundaries was similar with chemical composition of the Laves phase (Fig. 6b and c). These M_6C particles contained approximately 65 wt% W, 25% Fe and 10% Cr (Fig. 6).

The nucleation of the M_6C carbides on the $M_{23}C_6$/α-Fe surfaces provided the several ORs between the $M_{23}C_6$ and M_6C carbides (Fig. 3b). The M_6C composition was observed at one or two edges of the hybrid particles, in which the core and other edges consisted of the $M_{23}C_6$ composition. The relative crystallographic orientation of two carbides corresponds to the cube-on-cube OR (Fig. 3b), i.e. $(111)_{M23C6} \parallel (111)_{M6C}$, $(110)_{M23C6} \parallel (110)_{M6C}$ and $(001)_{M23C6} \parallel (001)_{M6C}$. The zone axes for the $M_{23}C_6$ carbide and M_6C carbide are $[1\bar{1}0]_{M23C6}$ and $[1\bar{1}0]_{M6C}$, respectively. This OR was observed after all creep regimes. In addition, a new OR between the $M_{23}C_6$ carbide and M_6C carbide was identified as:

$$(111)_{M23C6} \parallel (111)_{M6C}, \quad [\bar{1}2\bar{1}]_{M23C6} \parallel [\bar{1}10]_{M6C} \tag{5}$$

after 83 h of creep test (Fig. 3c-f). The lattice misfit (δ) between the $M_{23}C_6$ and M_6C carbides can be defined as [37,51]:

$$\delta = \frac{d_{M23C6} - d_{M6C}}{d_{M23C6}} \tag{6}$$

where d_{M23C6} and d_{M6C} are the interplanar spacing of the $M_{23}C_6$ and M_6C carbides, respectively. The lattice misfit between the $M_{23}C_6$ and M_6C carbides was calculated as 4.1% for the cube-on-cube OR and 4.3% for the OR by Eq. (5). The average size of the M_6C carbides nucleated on the $M_{23}C_6$/α-Fe interfaces comprised 23 nm (Fig. 5a) and, therefore, the $M_{23}C_6$/ M_6C surfaces were mostly incoherent and only minor part of these interfaces for rather fine M_6C nuclei could be semi-coherent.

The nucleation of the M_6C carbides on the $M_{23}C_6$/α-Fe interfaces changed the ORs between the $M_{23}C_6$ carbides and ferritic matrix. The $(111)_{M23C6}$ and $(111)_{M6C}$ planes in the $M_{23}C_6$ and M_6C carbides, respectively, became parallel to a $(001)_{\alpha\text{-Fe}}$ plane, and the zone axes for the $M_{23}C_6/M_6C$ carbides and ferritic matrix were $[1\bar{1}0]_{M23C6}$ and $[\bar{3}10]_{\alpha\text{-Fe}}$, respectively (Fig. 3b). This OR can be written as follows:

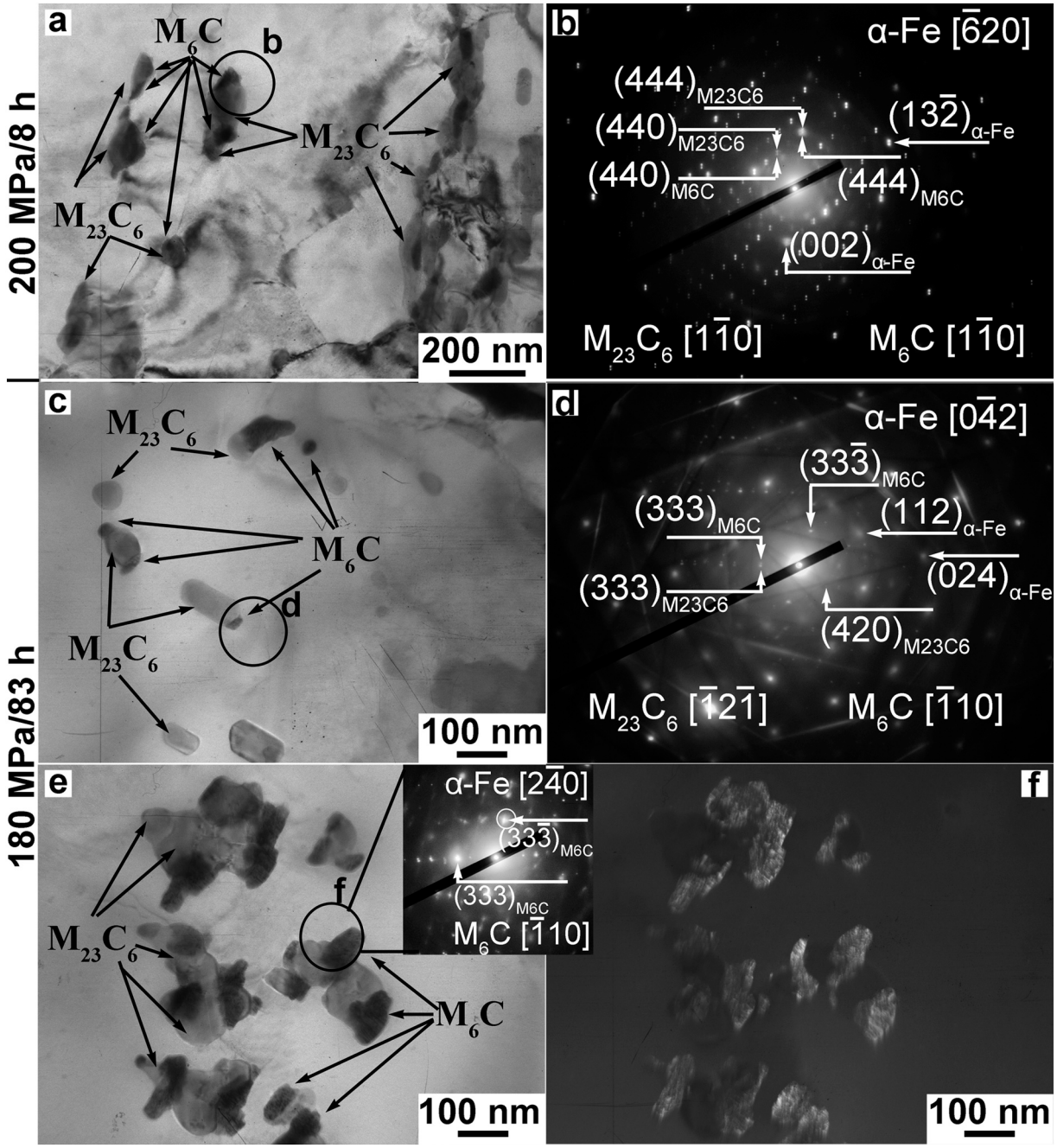

Fig. 3. Bright-field TEM image of foils showing the precipitation of M_6C carbides on the $M_{23}C_6$/ferrite surface (a,c,e) and electron diffraction patterns from M_6C carbide (b,d) with corresponding dark-field image in reflection of M_6C carbide (f). Circles in (a,c,e) show the places, which the electron diffraction patterns were taken from.

$$(111)_{M23C6} \parallel (111)_{M6C} \parallel (001)_{\alpha-Fe}, \quad [1\bar{1}0]_{M23C6} \parallel [1\bar{1}0]_{M6C} \parallel [\bar{3}10]_{\alpha-Fe} \tag{7}$$

The lattice misfits between the ferrite and $M_{23}C_6$ carbide as well as between the ferrite and M_6C carbide were 7.3% and 11.7%, respectively, for a $(001)_{\alpha\text{-Fe}}$ plane in Eq. (7) (Fig. 3b). Therefore, the nucleation of the M_6C carbides on the $M_{23}C_6$/α-Fe interfaces led to a loss of coherence of these interfaces. The $M_{23}C_6$/α-Fe or M_6C/α-Fe interfaces became fully incoherent. As a result, the coarsening of the M_6C carbides nucleated on the $M_{23}C_6$/ferrite interfaces occurred and their dimension increased up to 48 nm (Fig. 5c). A two-fold increase in the dimension of these M_6C carbides was attributed to the concurrent precipitation of new M_6C carbides and growth of the M_6C carbides precipitated during tempering. The ORs between the $M_{23}C_6$ carbide, M_6C carbide and ferrite defined by Eq. (7) retained with decreasing the applied stress.

The nucleation of M_6C carbides on the martensitic lath boundaries also occurred under creep (Fig. 4). These particles have a plate-like shape. At an applied stress of 200 MPa (8 h), their mean dimensions are 84 and 28 nm along the lath boundaries and in perpendicular direction, respectively. A decrease in the applied stress led to the highly increased dimension of these carbides along the lath boundaries, whereas the thickness increment was relatively low (Fig. 4). At an applied stress of 180 MPa (83 h), the longitudinal dimension attained 136 nm, whereas thickness comprised 36 nm. Therefore, the M_6C carbides grew along the lath boundaries under creep. This is attributed to the fact that the ORs between the M_6C carbides nucleated on the lath boundaries are distinctly different from that for these carbides nucleated on the $M_{23}C_6$/α-

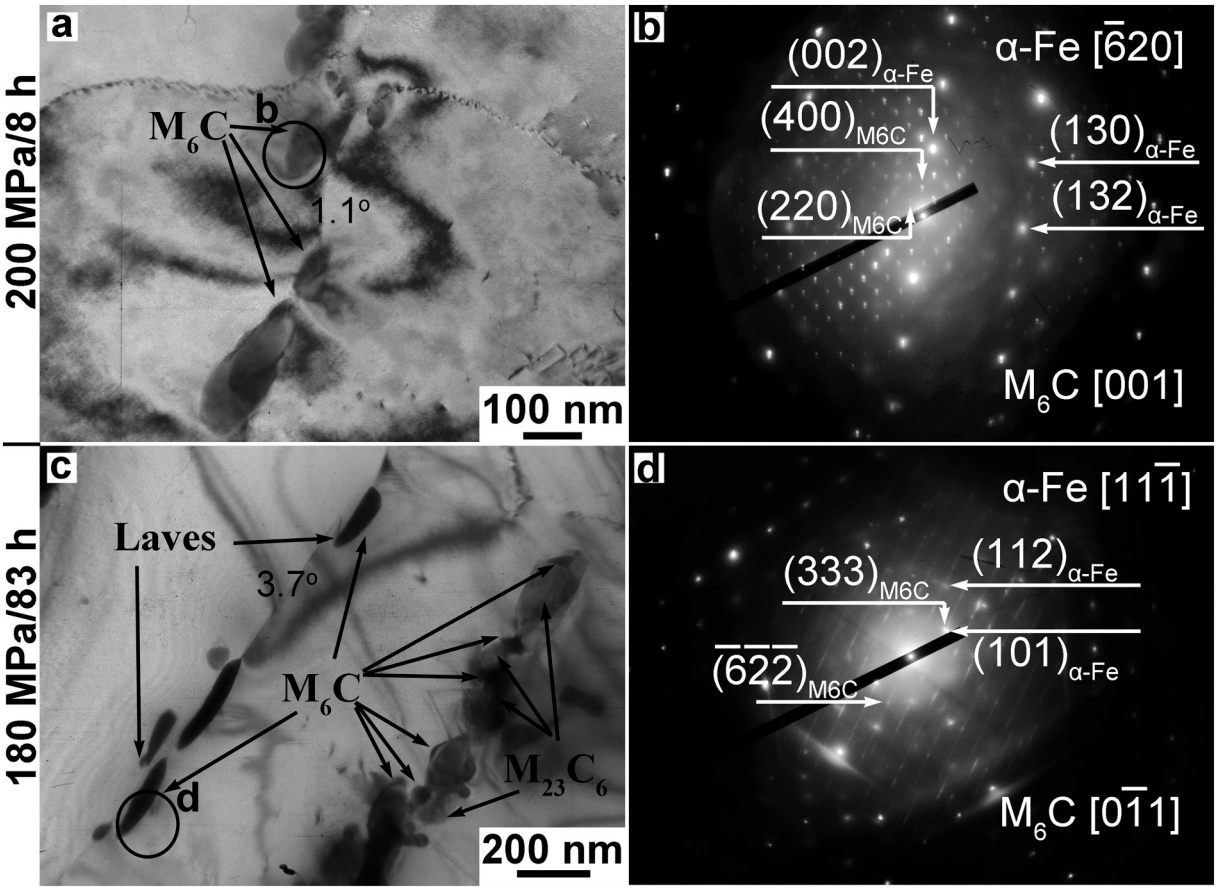

Fig. 4. Bright-field TEM image of foils showing the precipitation of M_6C carbides on the low-angle boundaries of the martensitic laths (a,c) and electron diffraction patterns from M_6C carbide (b,d). Circles in (a,c) show the places, which the electron diffraction patterns were taken from.

Fe interfaces (Figs. 3 and 4). The $(100)_{M6C}$ plane in the most of the M_6C carbides nucleated on the lath boundaries was parallel to a $(001)_\alpha$ plane, and the zone axis for the M_6C carbide and ferrite were $[001]_{M6C}$ and $[\bar{3}10]_\alpha$, respectively (Fig. 4b). Therefore, the OR can be written as follows:

$$(100)_{M6C} \parallel (001)_{\alpha-Fe}, \quad [001]_{M6C} \parallel [\bar{3}10]_{\alpha-Fe} \tag{8}$$

In addition, the following OR:

$$(\bar{3}\bar{1}7)_{M6C} \parallel (002)_{\alpha-Fe}, \quad [\bar{6}4\bar{1}]_{M6C} \parallel [\bar{3}10]_{\alpha-Fe} \tag{9}$$

was observed for several particles. The lattice misfits were 6.8% and 0.73% for the ORs by Eqs. (8) and (9), respectively. The M_6C/α-Fe interfaces along the lath boundaries exhibiting the OR by Eq. (9) were semi-coherent or coherent and, therefore, their interfacial energy was low. At an applied stress of 180 MPa, the OR between the M_6C carbides and ferrite close to the Kurdjumov-Sachs OR was found (Fig. 4d):

$$(111)_{M6C} \parallel (101)_\alpha, \quad [0\bar{1}1]_{M6C} \parallel [11\bar{1}]_\alpha \tag{10}$$

$$(773)_{M6C} \parallel (013)_\alpha, \quad [\bar{1}10]_{M6C} \parallel [03\bar{1}]_\alpha \tag{11}$$

$$(\bar{1}\bar{1}3)_{M6C} \parallel (100)_\alpha, \quad [\bar{1}10]_{M6C} \parallel [03\bar{1}]_\alpha \tag{12}$$

The lattice misfit δ for the $(101)_\alpha$ plane calculated by Eq. (3) was 1.1%, and for the $(013)_\alpha$ and $(100)_\alpha$ planes δ were 15 and 17%, respectively. This OR also caused a plate-like shape of M_6C carbides nucleated on the lath boundaries. It is worth noting that the SAED patterns taken from the M_6C carbides located on the $M_{23}C_6$/α-Fe interfaces contained numerous satellite spots and unclear streaks (Fig. 3b,d); the SAED patterns from the M_6C carbides located on the martensitic laths could contain well-defined streaks like Laves phase (Fig. 4d).

Thus, the nucleation of the M_6C carbides on the $M_{23}C_6$/α-Fe surfaces yields incoherency of both $M_{23}C_6$/α-Fe and M_6C/α-Fe interfaces. These carbides are susceptible to coarsening and their interfaces can serve as nucleation sites for the Laves phase. The M_6C carbide precipitation on the lath boundaries produces the particles with plate-like shape and semi-coherent longitudinal interface that are not favorable as the sites for the Laves phase nucleation. However, these plates are dissolved due to the precipitation and growth of the Laves phase, primarily. As a result, at an applied stress of 160 MPa, only the hybrid particles retain (Fig. 5g). The average size of these particles with nearly round shape attains approximately 80 nm. After 254 h of creep at 130 MPa, the dissolution of the M_6C carbides led to the formation of a one-peak distribution with an average size of these particles of 80 nm (Fig. 5e). The lacking of coarse M_6C particles larger than 150 nm confirms that the dissolution of the M_6C carbides nucleated on the lath boundaries is facilitated in comparison with hybrid particles. At an applied stress of 160 MPa, only hybrid particles were retained with size ranging from 50 to 100 nm (Fig. 5g). Their volume fraction was negligible. The maximum peak of volume fraction for M_6C carbides corresponded to the creep time of 83 h (Fig. 2a). During a longer creep, M_6C carbides begin to dissolve; Laves phase precipitates (Fig. 2a).

3.3. Precipitation of Laves Phase During Creep

At an applied stress of 180 MPa and less, the Laves phase particles were observed along the low-angle martensitic lath boundaries as thin elongated lamellas [26,40]. They precipitated both in contacts with the M_6C carbides, which were also located on the martensitic lath boundaries, and as the separate particles (Fig. 7). Therefore, a rod-like shape of Laves phase was associated with nucleation on the low energy semi-coherent carbide/ferrite interfaces or dislocation boundaries. Almost all

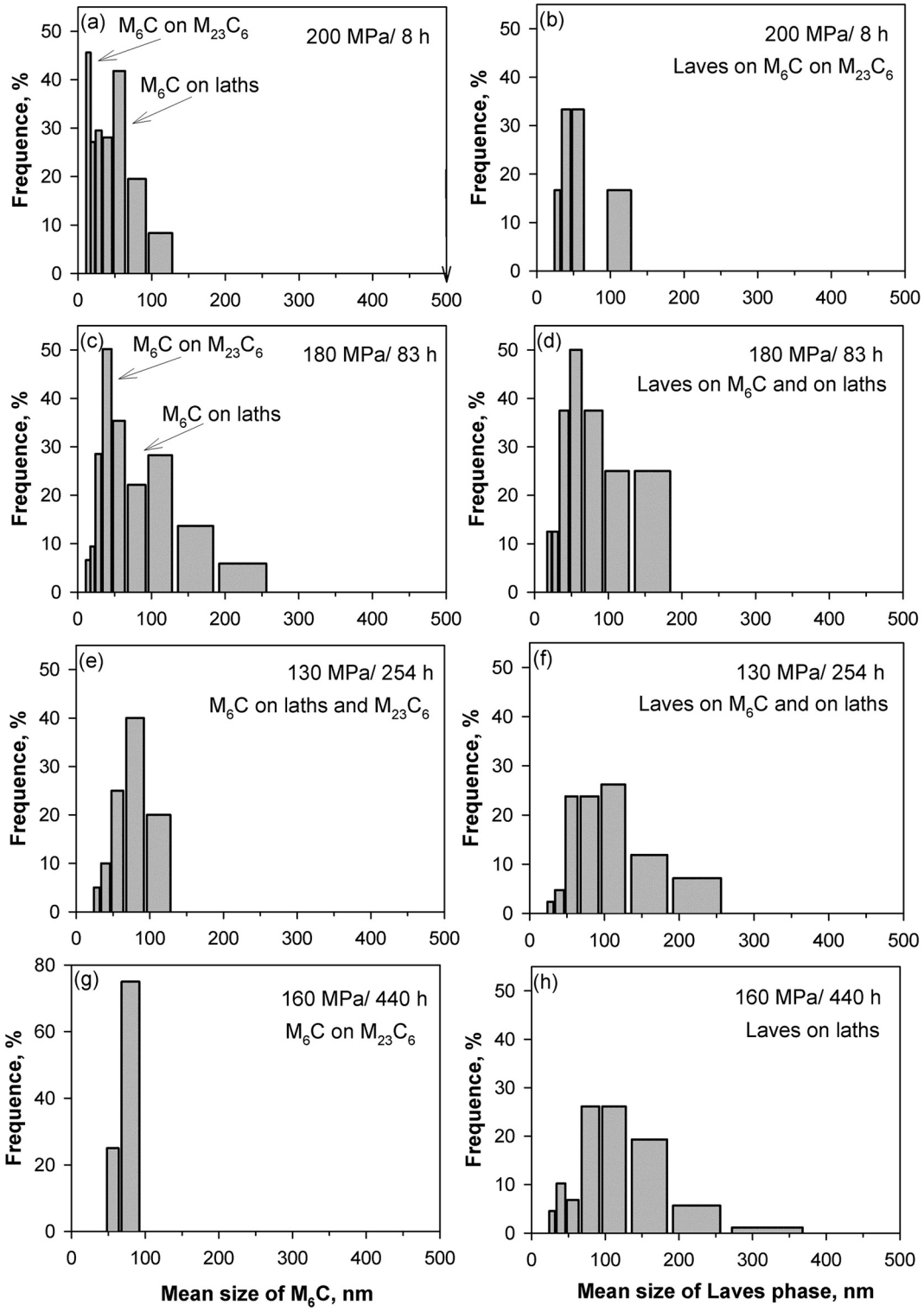

Fig. 5. Size distribution of M_6C carbide (a,c,e,g) and Laves phase particles (b,d,f,h) after creep tests at 650 °C/200 MPa (8 h to rupture) (a,b), 650 °C/180 MPa (83 h to rupture) (c,d), 650 °C/130 MPa (254 h) (e,f) and 650 °C/160 MPa (440 h to rupture) (g,h).

Laves phase particles exhibited the unique ORs [37] with ferrite, which could be described as follows:

$$(201)_{Laves} \parallel (112)_{\alpha-Fe}, \quad [\bar{1}\bar{6}2]_{Laves} \parallel [1\bar{1}1]_{\alpha-Fe} \text{ with } \delta = 14\% \tag{13}$$

$$(214)_{Laves} \parallel (011)_{\alpha-Fe}, \quad [\bar{1}\bar{6}2]_{Laves} \parallel [1\bar{1}1]_{\alpha-Fe} \text{ with } \delta = 16\% \tag{14}$$

$$(013)_{Laves} \parallel (112)_{\alpha-Fe}, \quad [\bar{1}\bar{6}2]_{Laves} \parallel [\bar{3}5\bar{1}]_{\alpha-Fe} \text{ with } \delta = 7\% \tag{15}$$

A high misfit value is indicative for the fact that the Laves/α-Fe interfaces of any particles with dimensions ≥20 nm are incoherent. It was noticed in the works [46,52,53], that the nuclei have the semi-coherent interface with one adjacent subgrain and incoherent interface with another adjacent subgrain. The Laves phase particles nucleated on the lath boundaries had the ORs described by Eqs. (13–15) with only one adjacent lath [40,52,53]. The OR with neighbor lath was deviated

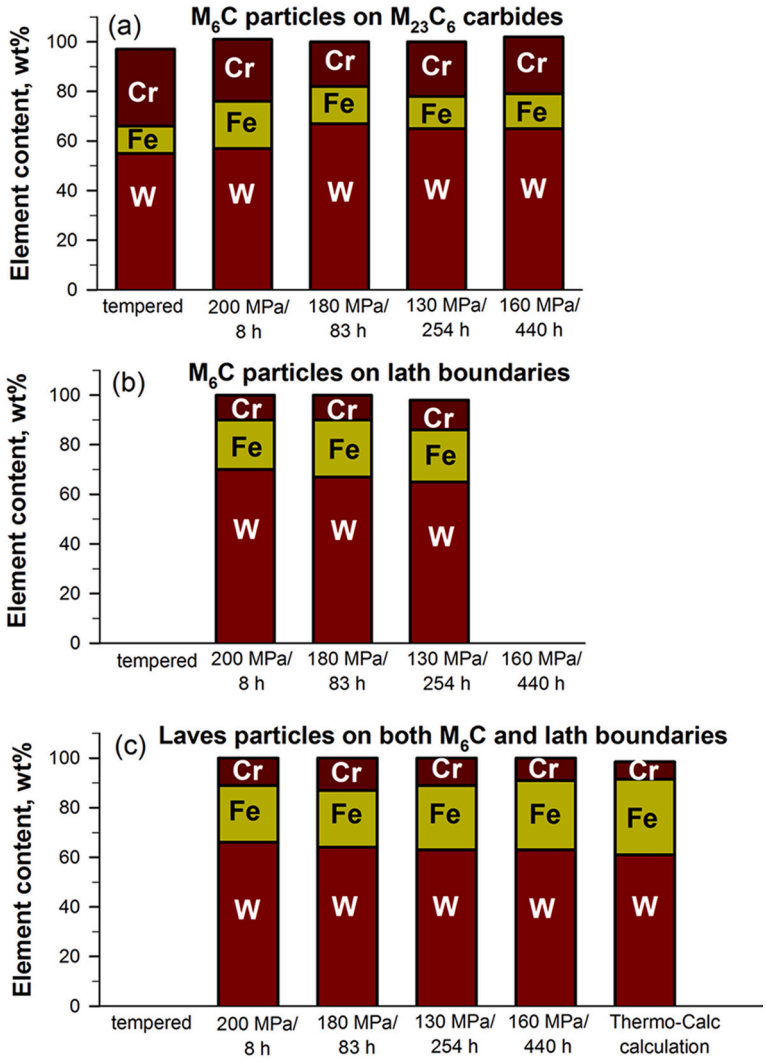

Fig. 6. The change in the chemical composition of the M_6C carbides located on the $M_{23}C_6$/ferrite surface (a) and on the martensitic laths (b) as well as that of Laves phase located on both the M_6C/ferrite surface and martensitic lath boundaries (c).

from the ORs described by Eqs. (13–15) by the amount of misorientation of the lath boundaries and, therefore, the misfit of this interface was higher. This is supported by results presented in Fig. 7a-c. A further growth of the Laves phase particles occurred toward the lath with an incoherent interface (Fig. 7d-f) [26,40,52]. A. Kipelova et al. [36] suggested that the elongated shape of these particles indicates a significant role of boundary diffusion in the precipitation process. As a result, the particles had the interface without OR and with a high interfacial energy from one side (Fig. 7c,f) and the interface with OR and lower energy from the opposite side (Fig. 7b.e), which could be written as:

$$(110)_{Laves} \parallel (101)_{\alpha-Fe}, \quad [1\bar{1}0]_{Laves} \parallel [1\bar{1}1]_{\alpha-Fe} \text{ with } \delta = 16\% \tag{16}$$

The growth of Laves phase occurred by migration of the last interface producing the bulky-shape Laves phase particles instead of rod-like shape particles (Fig. 7d,g). These particles were susceptible to coarsening. As a result, at 160 MPa, the major portion of Laves phase was the spheroidized particles (Fig. 7d). The average dimension of the Laves phase particles increased with decreasing applied stress (Fig. 5b,d,f,h).

After long-term creep for 10,987 h at 140 MPa, the coarse Laves phase particles lost the ORs with the ferritic matrix from both sides of semi-coherent and incoherent interfaces (Fig. 7g,h), while the Laves phase particles grew toward the subgrain with an incoherent interface until reaching their equilibrium volume fraction and chemical composition as also suggested by Sahnueza et al. [52]. At the same time, the fine Laves phase particles with an average size of 50 nm located on the low-angle boundaries of the martensitic laths demonstrated retaining the ORs with the ferritic subgrains (Fig. 8i), which could be written as follows:

$$(204)_{Laves} \parallel (002)_{\alpha-Fe}, \quad [010]_{Laves} \parallel [4\bar{6}0]_{\alpha-Fe} \text{ with } \delta = 2.3\% \tag{17}$$

There was another way to nucleate the Laves phase in the *Re*-containing 10% Cr-3% Co-3% W steel, which sometimes meets in the 9–12% Cr steels [40,48]. After 8 h of creep test at 200 MPa, the major portion of the Laves phase particles nucleated on the M_6C/α-Fe interfaces of the hybrid $M_6C/M_{23}C_6$ particles (Fig. 8a). Hybrid particles are preferential sites for heterogeneous nucleation of the Laves phase to form the equiaxed particles. The size distribution was characterized by a peak corresponding to the Laves phase particles with an average size of 70 nm (Fig. 5b). The volume fraction of these Laves phase particles was 0.02% (Fig. 2a). The dimensions of 85% of the Laves phase particles lay in the range of 25–75 nm (Fig. 5b). At an applied stress of 180 MPa, the ratio of the Laves phase nucleated on the M_6C/α-Fe surface and on the lath boundaries was 1: 1. A ten-fold increase in the volume fraction of the Laves phase up to 0.20% after 83 h of creep (Fig. 2a) led to the formation of a unimodal size distribution with one peak corresponding to the average size of these particles (70 nm) (Fig. 5d). The broadening of this distribution to larger dimensions is

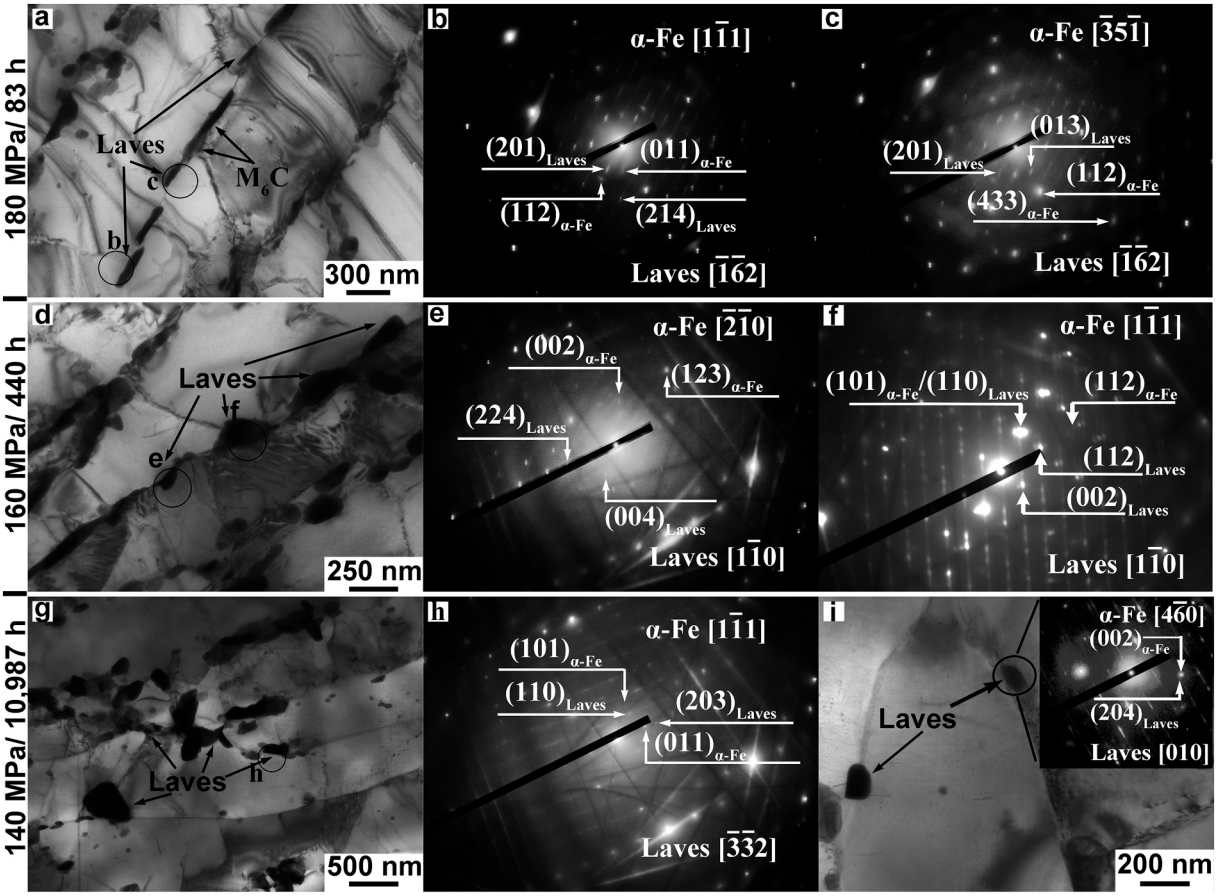

Fig. 7. Bright-field TEM image of foils showing the precipitation of Laves phase on the boundaries of the martensitic laths (a,d,g,i) and electron diffraction patterns from Laves phase (b,c,e,f,h). Circles in (a,d,g) show the places, which the electron diffraction patterns were taken from. Fine Laves phase retained the OR with matrix even after 10,987 h of creep at 650 °C/140 MPa (i).

associated with the Laves phase particles nucleated on the lath boundaries with or without contact with M_6C carbides (Fig. 7a-c). The M_6C carbides with plate-like shape located on the lath boundaries are replaced by the Laves phase particles [48] (Fig. 7a).

The Laves phase particles nucleated on the M_6C/α-Fe interfaces exhibited the following ORs (Fig. 8):

$$(103)_{Laves} \parallel (010)_{M6C}, \quad [\bar{3}\bar{5}1]_{Laves} \parallel [30\bar{5}]_{M6C} \tag{18}$$

$$(103)_{Laves} \parallel (010)_{M6C}, \quad [\bar{3}\bar{5}1]_{Laves} \parallel [30\bar{5}]_{M6C} \tag{19}$$

$$(103)_{Laves} \parallel (\bar{5}11)_{M6C}, \quad [0\bar{1}0]_{Laves} \parallel [2\bar{8}\ \bar{1}8]_{M6C} \tag{20}$$

$$(10\bar{3})_{Laves} \parallel (331)_{M6C}, \quad [0\bar{1}0]_{Laves} \parallel [2\bar{8}\ \bar{1}8]_{M6C} \tag{21}$$

$$(100)_{Laves} \parallel (\bar{1}21)_{M6C}, \quad [0\bar{1}0]_{Laves} \parallel [2\bar{8}\ \bar{1}8]_{M6C} \tag{22}$$

$$(214)_{Laves} \parallel (355)_{M6C}, \quad [441]_{Laves} \parallel [0\bar{1}1]_{M6C} \tag{23}$$

The lattice misfit δ between the Laves phase and M_6C carbides can be defined as [37,51]:

$$\delta = \frac{d_{M6C} - d_{Laves}}{d_{M6C}} \tag{24}$$

where d_{M6C} and d_{Laves} are the interplanar spacing of the M_6C carbide and Laves phase, respectively. These ORs were characterized by the high lattice misfits of 21–23% (Eqs. (18 and 19)), 14–16% (Eqs. (21 and 23)) and less than 10% (Eqs. (20 and 22)). At an applied stress of 180 MPa, a new OR between the Laves phase and M_6C carbide was revealed (Fig. 8e):

$$(112)_{Laves} \parallel (33\bar{3})_{M6C}, \quad [\bar{3}51]_{Laves} \parallel [\bar{3}41]_{M6C} \text{ with } \delta = 5.8\% \tag{25}$$

Therefore, all M_6C/Laves phase interfaces were incoherent. In a dark-field TEM image (Fig. 8f), both fine particles on the surface of other W-rich particles and the rim regions of M_6C carbides were illuminated. All diffraction patterns from the Laves phase located on the M_6C/α interface and lath boundaries contained the well-defined streaks (Figs. 7b,c,e,f,h and 8b,c,e,i).

The size of the Laves phase particles located on the M_6C/ferrite surface was smaller than that of these particles located on the martensitic lath boundaries (Figs. 5, 7 and 8). The growth of Laves phase particles by consuming M_6C carbides led to loss of the ORs. between the M_6C carbides and Laves phase after 440 h of creep test at 160 MPa (Fig. 8g-i). The chemical composition of Laves phase already after 8 h of creep was close to the equilibrium composition predicted by Thermo-Calc software; no significant changes in the chemical composition of Laves phase with increasing the creep time up to 440 h were revealed (Fig. 6c). No difference in the chemical compositions of Laves phase particles nucleated at different sites was observed (Fig. 6c).

3.4. $M_{23}C_6$ Carbide → M_6C Carbide → Laves Phase Transformation

TEM experimental results showed that nucleation of the Laves phase particles can occur not only heterogeneously at (sub)boundaries in the 9–12% Cr steels containing W and Co as it was suggested and shown in many works [9–15,18,19,21,22,26–41,43,44,46–50,52,53], but also through the metastable M_6C phase using the $M_{23}C_6$/α-Fe surface or the martensitic lath boundaries as nucleation sites. A precipitation sequence (1) retains [48]. The $M_{23}C_6$ carbides nucleate on the low- and high-angle boundaries during tempering, while the M_6C carbides precipitate during tempering and creep on the $M_{23}C_6$/α-Fe interfaces and

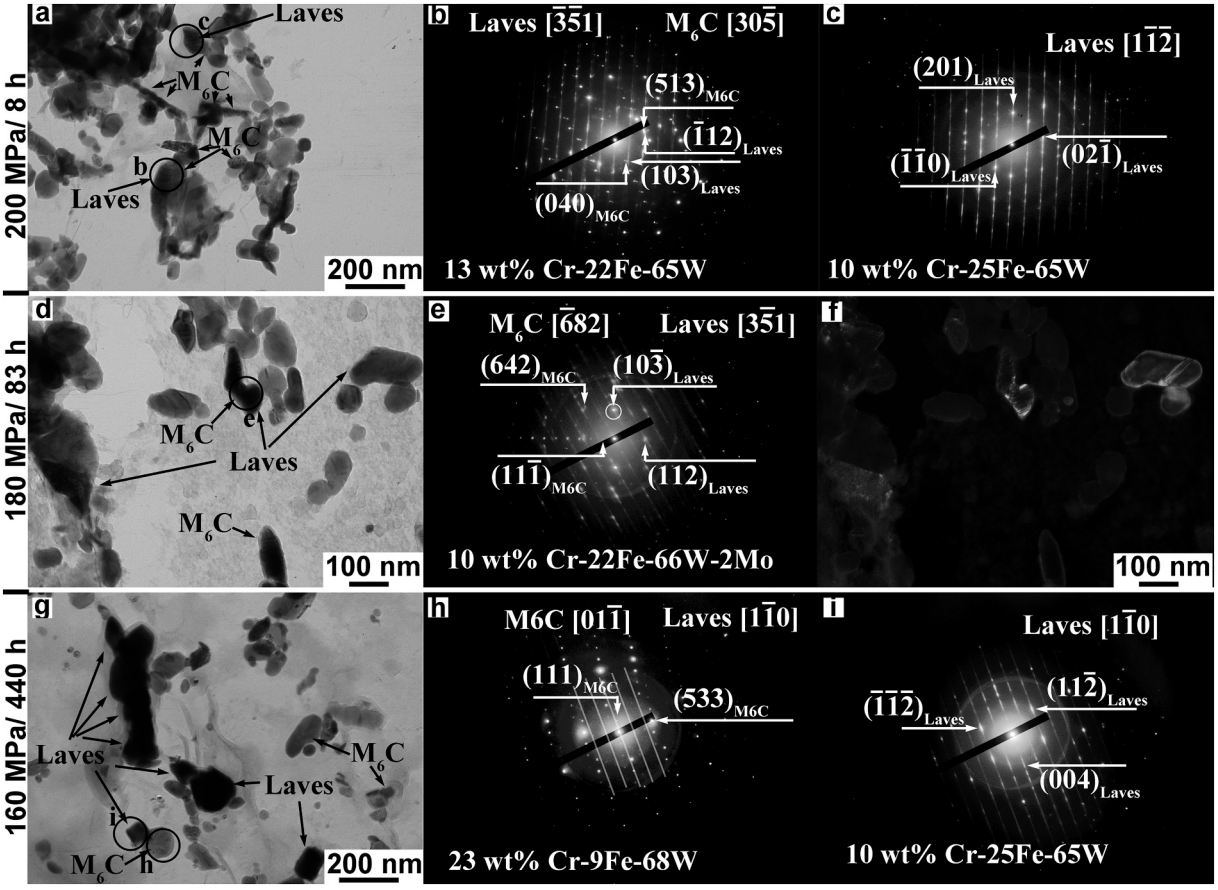

Fig. 8. Bright-field TEM image of foils showing the precipitation of Laves phase on M_6C/ferrite surface (a,d,g) and electron diffraction patterns from Laves phase (b,c,e,h,i) with corresponding dark-field image in reflection of Laves phase (f). Circles in (a,d,g) show the places, which the electron diffraction pattern was taken from. Lines in (h) showed the streaks from neighbor Laves phase.

on the lath boundaries. Moreover, the precipitation of the M_6C carbides in the 9–10% Cr-3% Co steels with different W content was reported in [45,48]. The nucleation of M_6C on the $M_{23}C_6$ carbides was reported in [54,55]. The cube-on-cube OR, i.e. $(111)_{M23C6} \parallel (111)_{M6C}$, $(110)_{M23C6} \parallel (110)_{M6C}$ and $(001)_{M23C6} \parallel (001)_{M6C}$, is observed in Ref. [54] and often meets in the steel studied. A. Inoue et al. [54] suggested that a small value of misfit (less than 5%) indicates the in-situ transformation, wherein $M_{23}C_6$ carbide is not a metastable phase and remains in the structure even after the dissolution of M_6C carbide and precipitation of Laves phase. $M_{23}C_6$ carbides play the role of a ready-to-use substrate with concentration of carbon close to that in M_6C carbides, while concentration of tungsten in M_6C carbide is significantly higher than that in $M_{23}C_6$ carbide. The diffusion of tungsten atoms from ferrite to resultant carbide is thought to be the process controlling the rate of M_6C precipitation.

The nucleation of the Laves phase particles occurs on the M_6C/α-Fe interfaces that induces the loss of coherency of the carbide/ferrite interfaces. The ORs between the M_6C carbide and Laves phase meet rarely [48], wherein the same OR of $(103)_{Laves} \parallel (\bar{5}11)_{M6C}$ (Eq. (20)) was observed in the present work. M. Isik et al. [26,40] and G. Dimmler et al. [56] showed the nucleation of the Mo-rich Laves phase on the Cr-rich $M_{23}C_6$/α-Fe surface or near $M_{23}C_6$ carbides. The formation of Laves phase particles near $M_{23}C_6$ carbides was related to the Si and P segregations surrounding the growing carbides [26,40]. In the present work, no Si or P segregations in the vicinity of $M_{23}C_6$ or M_6C carbides were revealed, and the formation of the Laves phase particles near the $M_{23}C_6$ carbides occurred through the previous formation of the M_6C carbide on the $M_{23}C_6$/α-Fe surface. The Laves phase nucleation on the M_6C/ferrite surface is an in-situ transformation accompanied by compositional changes due to the presence of carbon atoms in M_6C carbide. The M_6C carbides, like $M_{23}C_6$ carbides [54], act as a ready-to-use substrate for nucleation of Laves phase, wherein tungsten concentration in the M_6C carbide and Laves phase is similar and comprises approximately 60 wt%. This seems that the diffusion of tungsten from the matrix to the Laves phase and diffusion of excess chromium and carbon from the M_6C carbide to ferrite are the rate-controlling processes for the $M_6C \rightarrow$ Laves phase transformation. The orientation relationship of $(112)_{Laves} \parallel (11\bar{1})_{M6C}$ with a lattice misfit $\delta = 2.3\%$ is often met after 83 h of creep test at 180 MPa, at which the onset of the Laves phase precipitation occurs. Effect of the M_6C carbides and Laves phase on creep behavior is complicated [13,14,18,19,21,30,31,39,43]. The precipitation of the M_6C carbides can affect the growth of the Laves phase particles, since the nucleation of the M_6C carbides and Laves phase are competitive processes; and M_6C carbides occupy the potential W-rich nucleation sites that decreased the volume number density of Laves phase. At the same time, a high fraction of the Laves phase particles (as well as $M_{23}C_6$ carbides) located at the martensitic lath boundaries stabilizes the TMLS during creep and provides an enhanced creep resistance [23,25].

4. Conclusions

The precipitation of Laves phase occurs through $M_{23}C_6 \rightarrow M_6C \rightarrow$ Laves phase sequence in the *Re*-containing 10% Cr-3% Co-3% W steel. The main summary can be written as follows:

1. Tempering at 770 ˚C provides the formation of the tempered martensite lath structure with the mean transverse size of martensitic

laths of about 300 nm and high dislocation density in the lath interior. The $M_{23}C_6$ ($\bar{d}_{av}$ = 67 nm) and M_6C ($\bar{d}_{av}$ = 28 nm) carbides located along the boundaries of the martensitic laths as well as the Nb-rich MX carbonitrides ($\bar{d}_{av}$ = 37 nm) randomly distributed in the matrix have been revealed in the tempered state.

2. The $M_{23}C_6 \rightarrow M_6C$ transformation occurs through the nucleation on the $M_{23}C_6/\alpha$-Fe interfaces, which induces the appearance of the hybrid $M_6C/M_{23}C_6$ particles, and on the lath boundaries during tempering and creep tests at 650 °C/200 MPa (8 h) and 650 °C/180 MPa (83 h). The M_6C carbides precipitated on the $M_{23}C_6/\alpha$-Fe surface, in contrast to the M_6C carbides precipitated on the martensitic lath boundaries, have an approximately half the mean size and contain a twice higher the Cr content up to 20 wt%.
3. The M_6C and $M_{23}C_6$ carbides and ferrite have the mutual orientation relationships. The orientation relationships of $(111)_{M23C6} \parallel (111)_{M6C} \parallel (001)_{\alpha-Fe}$ type, as well as $(111)_{M6C} \parallel (101)_{\alpha-Fe}$, $(\bar{3}\bar{1}7)_{M6C} \parallel (001)_{\alpha-Fe}$ type with the lattice misfit of 1.1% and 0.73%, respectively, have been found.
4. The $M_6C \rightarrow$ Laves phase transformation occurs through the nucleation on the M_6C/α-Fe interfaces and on the martensitic lath boundaries. The M_6C/Laves phase particles have been detected after creep at 650 °C/180 MPa (83 h). The number ratio of Laves phase particles precipitated on the martensitic lath boundaries and M_6C/ferrite surface is 1: 1. The chemical composition of Laves phase particles does not depend on the nucleation sites and is close to an equilibrium composition predicted by the Thermo-Calc software.
5. Several orientation relationships have been observed between the M_6C carbide and Laves phase. The orientation relationship of $(112)_{Laves} \parallel (11\bar{1})_{M6C}$ with the lattice misfit δ = 2.3% often meets after creep at 650 °C/180 MPa (83 h), at which the onset of precipitation of the Laves phase takes place. The individual and fine Laves phase particles located on the lath boundaries retain the orientation relationship with ferrite even after 10,987 h of creep at 650 °C/140 MPa.

Data Availability

The raw/processed data required to reproduce these findings cannot be shared at this time as the data also forms part of an ongoing study.

Declaration of Competing Interest

The authors declare that they have no known competing financial interests or personal relationships that could have appeared to influence the work reported in this paper.

Acknowledgements

This study was financially supported by the Russian Science Foundation, under grant No. 19-73-10089. TEM analysis was performed by using an equipment at the Joint Research Center, «Technology and Materials», Belgorod National Research University.

References

[1] H.K.D.H. Bhadeshia, Design of ferritic creep-resistant steels, ISIJ Int. 41 (2001) 626–640, https://doi.org/10.2355/isijinternational.41.626.
[2] F. Abe, T.-U. Kern, R. Viswanathan, Creep-Resistant Steels, Woodhead Publishing, Cambridge, 2008.
[3] M. Fukuda, Y. Tsuda, K. Yamashita, Y. Shinozaki, T. Takahashi, Materials and design for advanced high temperature steam turbines, in: Hilton Head Island, South Carolina, R. Viswanathan, D. Gandy, K. Coleman (Eds.), Conf. Proc. Advances in Materials Technology for Fossil Power Plants, 25–28 Oct. 2004, ASM International, Materials Park, 2005, pp. 491–505.
[4] R. Viswanathan, W. Bakker, Materials for ultrasupercritical coal power plants – turbine materials: part II, J. Mater. Eng. Perform. 10 (2001) 96–101, https://doi.org/10.1361/105994901770345402.
[5] V. Knezevic, J. Balun, G. Sauthoff, G. Inden, A. Schneider, Design of martensitic/ferritic heat-resistant steels for application at 923 K with supporting thermodynamic modeling, Mater. Sci. Eng. A 477 (2008) 334–343, https://doi.org/10.1016/j.msea.2007.05.047.
[6] R.O. Kaybyshev, V.N. Skorobogatykh, I.A. Shchenkova, New martensitic steels for fossil power plant: creep resistance, Phys. Met. Metallogr. 109 (2010) 186–200, https://doi.org/10.1134/S0031918X10020110.
[7] H. Kitahara, R. Ueji, N. Tsuji, Y. Minamino, Crystallographic features of lath martensite in low-carbon steel, Acta Mater. 54 (2006) 1279–1288, https://doi.org/10.1016/j.actamat.2005.11.001.
[8] A. Kostka, K.-G. Tak, R.J. Hellmig, Y. Estrin, G. Eggeler, On the contribution of carbides and micrograin boundaries to the creep strength of tempered martensite ferritic steels, Acta Mater. 55 (2007) 539–550, https://doi.org/10.1016/j.actamat.2006.08.046.
[9] A. Fedoseeva, N. Dudova, R. Kaibyshev, Creep strength breakdown and microstructure evolution in a 3%Co modified P92 steel, Mater. Sci. Eng. A 654 (2016) 1–12, https://doi.org/10.1016/j.msea.2015.12.027.
[10] R. Mishnev, N. Dudova, R. Kaibyshev, On the origin of the superior long-term creep resistance of a 10% Cr steel, Mater. Sci. Eng. A 713 (2018) 161–173, https://doi.org/10.1016/j.msea.2017.12.066.
[11] R. Mishnev, N. Dudova, A. Fedoseeva, R. Kaibyshev, Microstructural aspects of superior creep resistance of a 10%Cr martensitic steel, Mater. Sci. Eng. A 678 (2016) 178–189, https://doi.org/10.1016/j.msea.2016.09.096.
[12] F. Abe, Coarsening behavior of lath and its effect on creep rates in tempered martensitic 9Cr-W steels, Mater. Sci. Eng. A 387-389 (2004) 565–569, https://doi.org/10.1016/j.msea.2004.01.057.
[13] N. Dudova, A. Plotnikova, D. Molodov, A. Belyakov, R. Kaibyshev, Structural changes of tempered martensitic 9%Cr–2%W–3%co steel during creep at 650 °C, Mater. Sci. Eng. A 534 (2012) 632–639, https://doi.org/10.1016/j.msea.2011.12.020.
[14] V. Dudko, A. Belyakov, D. Molodov, R. Kaibyshev, Microstructure evolution and pinning of boundaries by precipitates in a 9pctCr heat resistant steel during creep, Metall. Mater. Trans. A 44 (2013) 162–172, https://doi.org/10.1007/s11661-011-0899-1.
[15] E. Tkachev, A. Belyakov, R. Kaibyshev, Creep strength breakdown and microstructure in a 9%Cr steel with high B and low N contents, Mater. Sci. Eng. A 772 (2020) 138821, https://doi.org/10.1016/j.msea.2019.138821.
[16] H.K. Danielsen, P.E. Di Nunzio, J. Hald, Kinetics of Z-phase precipitation in 9 to 12 pct Cr steels, Metall. Mater. Trans. A 44 (2013) 2445–2452, https://doi.org/10.1007/s11661-012-1583-9.
[17] L. Cipolla, H.K. Danielsen, D. Venditti, P.E. Di Nunzio, J. Hald, M.A.J. Somers, Conversion of MX nitrides to Z-phase in a martensitic 12% Cr steel, Acta Mater. 58 (2010) 669–679, https://doi.org/10.1016/j.actamat.2009.09.045.
[18] F. Abe, Effect of fine precipitation and subsequent coarsening of Fe_2W Laves phase on the creep deformation behavior of tempered martensitic 9Cr-W steels, Metall. Trans. A. 36A (2005) 321–332, https://doi.org/10.1007/s11661-005-0305-y.
[19] F. Abe, Progress in creep-resistant steels for high efficiency coal-fired power plants, J. Press. Vessel. Technol. 138 (2016) 040804, , https://doi.org/10.1115/1.4032372.
[20] P. Prakash, J. Vanaja, N. Srinivasan, P. Parameswaran, G.V.S. Nageswara Rao, K. Laha, Effect of thermo-mechanical treatment on tensile properties of reduced activation ferritic-martensitic steel, Mater. Sci. Eng. A 724 (2018) 171–180, https://doi.org/10.1016/j.msea.2018.03.080.
[21] A. Fedoseeva, N. Dudova, R. Kaibyshev, A. Belyakov, Effect of tungsten on creep behavior of 9%Cr–3%Co martensitic steels, Metals 7 (2017) 573, https://doi.org/10.3390/met7120573.
[22] F. Abe, T. Ohba, H. Miyazaki, Y. Toda, M. Tabuchi, Effect of W-Mo balance on long-term creep life of 9Cr steel, Mater. High Temp. 36 (2019) 314–324, https://doi.org/10.1080/09603409.2018.1555202.
[23] A. Fedoseeva, I. Nikitin, N. Dudova, R. Kaibyshev, Superior creep resistance of a high-Cr steel with Re additives, Mater. Lett. 262 (2020) 127183, https://doi.org/10.1016/j.matlet.2019.127183.
[24] T. Kunieda, K. Yamashita, Y. Murata, T. Koyama, M. Morinaga, Effect of rhenium of tungsten diffusivity in iron-chromium alloys, Mater. Trans. 47 (2006) 2106–2108, https://doi.org/10.2320/matertrans.47.2106.
[25] A. Fedoseeva, I. Nikitin, N. Dudova, R. Kaibyshev, On effect of rhenium on mechanical properties of a high-Cr creep resistant steel, Mater. Lett. 269 (2019) 81–84, https://doi.org/10.1016/j.matlet.2018.10.081.
[26] M.I. Isik, A. Kostka, V.A. Yardley, K.G. Pradeep, M.J. Duarte, P.P. Choi, D. Raabe, G. Eggeler, The nucleation of Mo-rich Laves phase particles adjacent to $M_{23}C_6$ micrograin boundary carbides in 12% Cr tempered martensite ferritic steels, Acta Mater. 90 (2015) 94–104, https://doi.org/10.1016/j.actamat.2015.01.027.
[27] Q. Lu, W. Xu, S. Zwaag, The computational design of W and Co-containing creep-resistant steels with barely coarsening Laves phase and $M_{23}C_6$ as the strengthening precipitates, Metall. Mater. Trans. A 45 (2014) 6067–6074, https://doi.org/10.1007/s11661-014-2557-x.
[28] Zh. Liua, Zh. Liu, X. Wang, Zh. Chen, Investigation of the microstructure and strength in G115 steel with the different concentration of tungsten during creep test, Mater. Charact. 149 (2019) 95–104, https://doi.org/10.1016/j.matchar.2019.01.015.
[29] H. Cui, F. Sun, K. Chen, L. Zhang, R. Wan, A. Shan, J. Wu, Precipitation behavior of Laves phase in 10%Cr steel X12CrMoWVNbN10-1-1 during short-term creep exposure, Mater. Sci. Eng. A 527 (2010) 7505–7509, https://doi.org/10.1016/j.msea.2010.08.013.
[30] O. Prat, J. Garcia, D. Rojas, G. Sauthoff, G. Inden, The role of Laves phase on microstructure evolution and creep strength of novel 9%Cr heat resistant steels, Intermetallics 32 (2013) 362–372, https://doi.org/10.1016/j.intermet.2012.08.

016.
[31] A. Fedoseeva, N. Dudova, R. Kaibyshev, Effect of stresses on the structural changes in high-chromium steel upon creep, Phys. Met. Metallogr. 118 (2017) 591–600, https://doi.org/10.1134/S0031918X17040032.
[32] V. Dudko, A. Belyakov, R. Kaibyshev, Evolution of lath substructure and internal stresses in a 9% Cr steel during creep, ISIJ Int. 57 (2017) 540–549, https://doi.org/10.2355/isijinternational.ISIJINT-2016-334.
[33] N. Dudova, R. Mishnev, R. Kaibyshev, Creep behavior of a 10%Cr heat-resistant martensitic steel with low nitrogen and high boron contents at 650 °C, Mater. Sci. Eng. A 766 (2019) 138353, https://doi.org/10.1016/j.msea.2019.138353.
[34] M. Mitsuhara, S. Yamasaki, M. Miake, H. Nakashima, M. Nishida, J. Kusumoto, A. Kanaya, Creep strengthening by lath boundaries in 9Cr ferritic heat-resistant steel, Philos. Mag. Lett. 96 (2016) 76–83, https://doi.org/10.1080/09500839.2016.1154200.
[35] Q. Gao, Y. Zhang, H. Zhang, H. Li, F. Qu, J. Han, C.H. Lu, B. Wu, Y. Lu, Y. Ma, Precipitates and particles coarsening of 9Cr–1.7W–0.4Mo–Co ferritic heat-resistant steel after isothermal aging, Sci. Rep. 7 (2017) 5859, https://doi.org/10.1038/s41598-017-06191-2.
[36] A. Kipelova, A. Belyakov, R. Kaibyshev, Laves phase evolution in a modified P911 heat resistant steel during creep at 923K, Mater. Sci. Eng. A 532 (2012) 71–77, https://doi.org/10.1016/j.msea.2011.10.064.
[37] I. Fedorova, A. Belyakov, P. Kozlov, V. Skorobogatykh, I. Shenkova, R. Kaibyshev, Laves phase precipitates in a low-carbon 9%Cr martensitic steel during ageing and creep at 923K, Mater. Sci. Eng. A 615 (2014) 153–163, https://doi.org/10.1016/j.msea.2014.07.046.
[38] X. Wang, Q. Xu, S.H. Yu, L. Hu, H. Liu, Y. Ren, Laves-phase evolution during aging in 9Cr-1.8W-0.5Mo-VNb steel for USC power plants, Mater. Chem. Phys. 163 (2015) 219–228, https://doi.org/10.1016/j.matchemphys.2015.07.032.
[39] L. Maddi, G.S. Deshmukh, A.R. Ballal, D.R. Peshwe, R.K. Paretkar, K. Laha, M.D. Mathew, Effect of Laves phase on the creep rupture properties of P92 steel, Mater. Sci. Eng. A 668 (2016) 215–223, https://doi.org/10.1016/j.msea.2016.05.074.
[40] M.I. Isik, A. Kostka, G. Eggeler, The nucleation of Laves phase particles during high-temperature exposure and creep of tempered martensite ferritic steels, Acta Mater. 81 (2014) 230–240, https://doi.org/10.1016/j.actamat.2014.08.008.
[41] N. Saini, R.S. Mulik, M.M. Mahapatra, Study on the effect of ageing on laves phase evolution and their effect on mechanical properties of P92 steel, Mater. Sci. Eng. A 716 (2018) 179–188, https://doi.org/10.1016/j.msea.2018.01.035.
[42] K.G. Abstoss, S. Schmigalla, S. Schultze, P. Mayr, Microstructural changes during creep and aging of a heat resistant MARBN steel and their effect on the electrochemical behavior, Mater. Sci. Eng. A 743 (2019) 233–242, https://doi.org/10.1016/j.msea.2018.11.075.
[43] K. Sawada, M. Takeda, K. Maruyama, R. Ishii, M. Yamada, Y. Nagae, R. Komine, Effect of W on recovery of lath structure during creep of high chromium martensitic steels, Mater. Sci. Eng. A 267 (1999) 19–25, https://doi.org/10.1016/S0921-5093(99)00066-0.
[44] B. Xiao, L. Xu, L. Zhao, H. Jing, Y. Han, Zh. Tang, Microstructure evolution and fracture mechanism of a novel 9Cr tempered martensite ferritic steel during short-term creep, Mater. Sci. Eng. A 707 (2017) 466–477, https://doi.org/10.1016/j.msea.2017.09.086.
[45] A. Fedoseeva, N. Dudova, U. Glatzel, R. Kaibyshev, Effect of W on tempering behaviour of a 3%Co modified P92 steel, J. Mater. Sci. 51 (2016) 9424–9439, https://doi.org/10.1007/s10853-016-0188-x.
[46] A. Fedoseeva, E. Tkachev, V. Dudko, N. Dudova, R. Kaibyshev, Effect of alloying on interfacial energy of precipitation/matrix in high-chromium martensitic steels, J. Mater. Sci. 52 (2017) 4197–4209 https://doi.org/10.1007/s10853-016-0654-5.
[47] V. Thomas Paul, V.D. Vijayanand, C. Sudha, S. Saroja, Effect of tungsten on long-term microstructural evolution and impression creep behavior of 9Cr reduced activation ferritic/martensitic steel, Metall. Mater. Trans. A 48 (2017) 425–438 https://doi.org/10.1007/s11661-016-3823-x.
[48] N. Dudova, R. Kaibyshev, On the precipitation sequence in a 10%Cr steel under tempering, ISIJ Int. 51 (2011) 826–831, https://doi.org/10.2355/isijinternational.51.826.
[49] E. Tkachev, A. Belyakov, R. Kaibyshev, Creep behavior and microstructural evolution of a 9%Cr steel with high B and low N contents, Mater. Sci. Eng. A 725 (2018) 228–241, https://doi.org/10.1016/j.msea.2018.04.032.
[50] V.A. Dudko, A.E. Fedoseeva, A.N. Belyakov, R.O. Kaibyshev, Influence of the carbon content on the phase composition and mechanical properties of P92-type steel, Phys. Met. Metallogr. 116 (2015) 1165–1174, https://doi.org/10.7868/S0015323015110054.
[51] A. Kipelova, A. Belyakov, R. Kaibyshev, The crystallography of M23C6 carbides in a martensitic 9% Cr steel after tempering, aging and creep, Philos. Mag. 93 (2013) 2259–2268, https://doi.org/10.1080/14786435.2013.765995.
[52] J.P. Sanhueza, D. Rojas, O. Prat, J. Garcia, M.F. Melendrez, S. Saurez, Investigation of Ta-MX/Z-phase and Laves phase as precipitation hardening particles in a 12 pct Cr heat-resistant steel, Metall. Mater. Trans. A 49 (2018) 2951–2962, https://doi.org/10.1007/s11661-018-4654-8.
[53] D. Rojas, J. Garcia, O. Prat, C. Carrasco, G. Sauthoff, A.R. Kaysser-Pyzalla, Design and characterization of microstructure evolution during creep of 12% Cr heat resistant steels, Mater. Sci. Eng. A 527 (2010) 3864–3876, https://doi.org/10.1016/j.msea.2010.02.056.
[54] A. Inoue, T. Masumoto, Carbide reactions ($M_3C \rightarrow M_7C_3 \rightarrow M_{23}C_6 \rightarrow M_6C$) during tempering of rapidly solidified high carbon Cr-W and Cr-Mo steel, Metall. Trans. A. 11A (1980) 739–747, https://doi.org/10.1007/BF02661203.
[55] B.A. Marinkovich, R.R. de Avilezz, S.K. Barros, F. Rizzo, Thermodynamic evaluation of carbide precipitates in 2.25Cr- 1.0Mo steel for determination of service degradation, Mater. Res. 5 (2002) 491–495, https://doi.org/10.1590/S1516-14392002000400016.
[56] G. Dimmler, P. Weinert, E. Kozeschnik, H. Cerjak, Quantification of the Laves phase in advanced 9-12%Cr steels using a standard SEM, Mater. Charact. 51 (2003) 341–352, https://doi.org/10.1016/j.matchar.2004.02.003.